


## Article

# Wing Load and Angle of Attack Identification by Integrating Optical Fiber Sensing and Neural Network Approach in Wind Tunnel Test

Daichi Wada \*  and Masato Tamayama

Aeronautical Technology Directorate, Japan Aerospace Exploration Agency, 6-13-1 Osawa, Mitaka-shi, Tokyo 181-0015, Japan; tamayama.masato@jaxa.jp

\* Correspondence: wada.daichi@jaxa.jp; Tel.: +81-50-3362-5566

Received: 18 March 2019; Accepted: 2 April 2019; Published: 8 April 2019



**Abstract:** The load and angle of attack (AoA) for wing structures are critical parameters to be monitored for efficient operation of an aircraft. This study presents wing load and AoA identification techniques by integrating an optical fiber sensing technique and a neural network approach. We developed a 3.6-m semi-spanned wing model with eight flaps and bonded two optical fibers with 30 fiber Bragg gratings (FBGs) each along the main and aft spars. Using this model in a wind tunnel test, we demonstrate load and AoA identification through a neural network approach. We input the FBG data and the eight flap angles to a neural network and output estimated load distributions on the eight wing segments. Thereafter, we identify the AoA by using the estimated load distributions and the flap angles through another neural network. This multi-neural-network process requires only the FBG and flap angle data to be measured. We successfully identified the load distributions with an error range of  $-1.5$ – $1.4$  N and a standard deviation of  $0.57$  N. The AoA was also successfully identified with error ranges of  $-1.03$ – $0.46^\circ$  and a standard deviation of  $0.38^\circ$ .

**Keywords:** fiber Bragg grating (FBG); load identification; machine learning; neural network; optical fiber sensor; structural monitoring

## 1. Introduction

Load monitoring techniques for wing structures are a promising technology for enhancing the flight performance of future aircrafts. Load monitoring is beneficial in terms of structural safety and reliability. There has been significant demand for high-aspect-ratio wings for efficient long-endurance flight, and the loading for such structurally challenging designs is critical [1]. Monitoring results of loading history can be utilized for structural fatigue analysis. By controlling applied loads to wings based on real-time load monitoring, it could be feasible to alleviate undesirable large moments at the wing root. When wings are flexible, aerodynamic loads cause large deflections, which affect the aeroelastic stability and response [2–4]. Load monitoring is beneficial to estimate structural deformation and conduct reliable structural analysis based on practical assumptions of deflected wing shape. Another potential benefit of load monitoring is stable and efficient control of an aircraft, including unmanned air vehicles (UAVs). Considering the gust perturbation process for example, the load variations from oncoming gusts result in attitude and flight path variations, and there is a theoretical phase-lag between the cause (load) and effect (attitude and flight path) [5–7]. The load is a “phase-advanced” phenomena in this sense, and, therefore, its observation in addition to the conventional inertia observations could potentially enhance vehicle controllability.

Aerodynamic loads are not always directly measurable. The wing structure is complex and space in wings is limited. It is difficult to install sufficient pressure sensors and tubes. To overcome

these engineering obstacles, studies have been conducted to estimate, as opposed to directly measure, the loads using a measurable parameter, which is a strain. In a mechanical sense, load causes strain. When strain is used to identify loads, it creates an inverse problem [8–10]. Inverse analyses tend to be ill-conditioned, specifically when distributed aerodynamic loads are to be calculated. The solution becomes highly unstable for the strain measurement errors. There have been a number of studies to obtain stable solutions. For example, using the inverse interpolation method, Shkarayev et al. assumed polynomial functions, whereas Coates et al. used Fourier cosine series terms for spatial load distribution functions [11,12]. Nakamura et al. reported a finite-element-based inverse analysis in which aerodynamic restriction was coupled with elastic equations [13]. These techniques to assume functions for aerodynamic load distributions are effective in improving the identification accuracy. There have been other studies to identify loads by using neural networks. Using strain as an input and load as an output of the neural network, the strain-to-load transfer is represented by the neural network that is optimized through a learning algorithm. The optimization through a learning algorithm contributes to stable solutions. Cao et al. conducted numerical simulations of a cantilever beam to validate the neural network applicability [14]. Trivailo et al. used strain gauge data to estimate loads in fatigue tests that simulated maneuver and buffet loads [15]. They reported successful results, although they focused primarily on the load identification in the form of a limited number of concentrated forces. Wada et al. reported that the approach was applicable for the identification of distributed loads by using a number of strain gauges bonded on a flat panel [16]. These techniques remain limited to a level of conceptual demonstration, and validation of the applicability in the aerodynamic environment needs to be conducted. Currently, one of the primary challenges is the collection of sufficient amounts of strain data from the wing structure under flight conditions.

It is not practical to install a myriad strain gauges on the surface of the wings considering the amount of wiring required. The digital image correlation technique would be a candidate to efficiently observe strain distribution profiles and there is a successful example of measuring strains for load estimation of membrane wings in wind tunnel tests [17]; however, some difficulties arise for in-flight uses. Stable setup of observation devices is not always available specifically when small UAVs are assumed and the observed images are under strong influence of flight environments such as the weather. On the other hand, recent studies indicate that optical fiber sensors are potentially promising techniques for obtaining strain information. By measuring multiple strains in a distributed manner along a single fiber, optical fiber-sensing exhibits significant effectiveness for collecting great volumes of data for wing and blade structures [18,19]. The sensing fibers are lightweight, thin, and can be attached to the surface of wings with only a marginal effect on the flight performance. A number of studies have demonstrated the feasibility of monitoring wings in wind tunnel tests [20] and UAV wings in flight using fiber Bragg gratings (FBGs) [21–23]. Multiple FBGs inscribed along fibers successfully measured strain distributions and enabled discussions about usage conditions, such as wing deformation.

In this study, by using optical fiber sensors, we conduct practical and efficient strain monitoring of a wing structure under actual aerodynamic loading conditions. Furthermore, we propose an integration of the strain monitoring technique and the neural network approach for load identification and investigate its applicability through an experimental demonstration in a wind tunnel test. A 3.6-m semi-spanned high-aspect-ratio wing model, with eight flaps on the trailing edge that enable arbitrary variations of load distributions, was developed. Two optical fibers with 30 FBGs each were bonded along the main and aft spars and measured strain distributions in a wavelength-division-multiplexing manner [24]. Aerodynamic loads were applied in a wind tunnel, and load distributions were identified by using the FBG and data from the eight flap angles through a neural network.

We discussed both structural and aerodynamic problems to which neural networks could be applied, based on which we proposed and examined another parameter identification, the angle of attack (AoA). The AoA is also one of the essential parameters that has a significant effect on the static and dynamic response of high-aspect-ratio wings [2–4]. We introduce an identification process for loads and AoAs that require only the FBG and flap angle data to be measured. We illustrate

the applicability of the optical fiber sensing and neural network through experimental results and discussions and demonstrate the effect of their integration for wing structures.

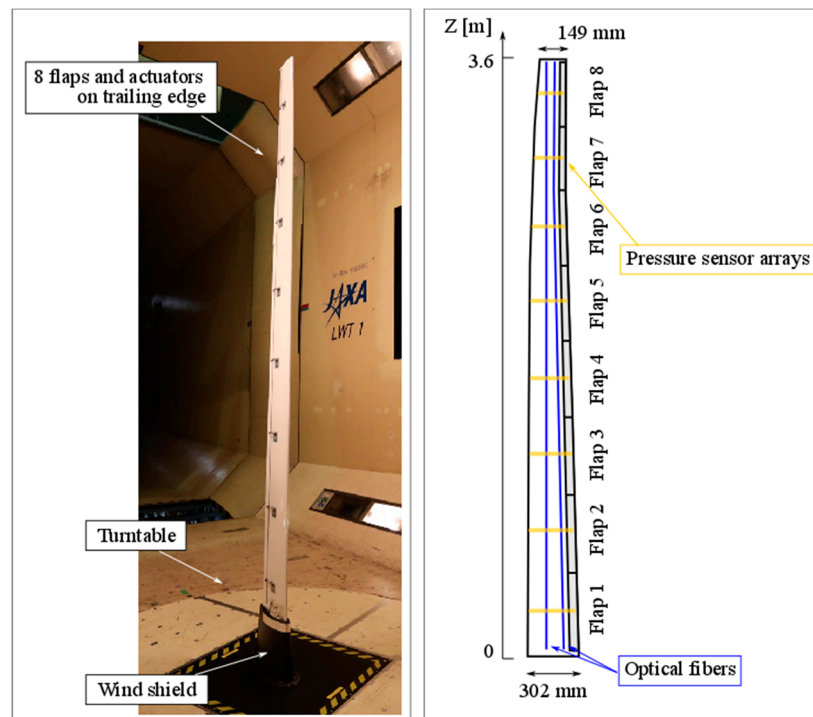
## 2. Materials and Methods

### 2.1. Wing Model with Multiple Flaps and Optical Fiber Sensors

We developed a 3.6-m semi-spanned wing model with eight flaps on the trailing edge. The wing structure had balsa wood main and aft spars and skin. Woven carbon fiber-reinforced plastic fabrics covered the balsa wood. A 400-mm stainless-steel shaft was inserted from the wing root in the main spar in order to attach the wing model to the wind tunnel base. Figure 1 shows a photograph and a schematic of the wing model. We set the Z axis along the span. We labelled the flaps Flap 1, 2, ..., 8 from the wing root. For each wing segment with Flap 1, 2, ..., 8, we listed in Table 1 the position Z of the center of the flap, the span-wise length of the flaps, the chord length of the wing measured at the center of the flaps, and the flap width measured in chord-wise. Servomotors (BLS177SV, Futaba) controlled the flap angles. The movable range of the flap angles was from  $-15^{\circ}$ – $15^{\circ}$ . The positive angle indicates flap down so that the lift force increases, with zero degrees being the neutral setting. We set eight static pressure-port arrays at the center of each wing segment. For each pressure sensor array, there were 15 pressure ports on the upper side and 8 on the lower side. A total of 184 silicon tubes for pressure sensors were installed and connected to an interrogator (Electronic Pressure Scanners, Pressure System) that was placed out of the wind tunnel. Figure 2 shows the cross-section of the wing model with the locations of the pressure ports and spars. We set the X and Y axes. We labelled the pressure ports on the upper side as  $u_1, u_2, \dots, u_{15}$  and on the lower side as  $l_1, l_2, \dots, l_8$ , counting from the leading edge. The normal direction at each pressure port was expressed by  $\theta$ . Table 2 listed the geometry of the pressure ports at the wing segment of Flap 1. The geometry was not identical but similar for other wing segments. The distributions of the pressure coefficient,  $C_p$ , of the wing segment with Flap 1 are shown in Figure 3. The flap position was neutral. We calculated the applied lift loads on each wing segment by integrating the measured static pressures around the airfoil. By dividing the airfoil into segments as labelled U1, U2, ..., U15, L1, L2, ..., L8 corresponding to each pressure port as seen in Figure 2, we multiplied the measured pressures with corresponding areas of the segments based on the approximation that the pressures were uniform in the segments. By considering the normal direction, we calculated the out-of-plane forces on the wing and defined them as the lift loads. Figure 4 shows the lift coefficient,  $C_L$ , of the wing model with respect to AoA. The positions of the flaps were neutral.

We bonded two optical fibers with inscribed FBGs on the upper side of the wing along the main and aft spars. We used an epoxy adhesive and fully covered the fibers with the minimum possible thickness. We applied a small pre-strain to set the fibers straight before bonding. We inscribed 30 FBGs at 120 mm intervals in individual fibers in order to cover the whole semi-span of the wing. The gauge length of the FBGs was 5 mm and the reflectivity was 70%. We designed the Bragg wavelengths of the 30 FBGs ranging from 1530–1595 nm (in the C- and L-bands) so that we could monitor the individual Bragg spectra in the wavelength-division-multiplexing manner. Figure 5 shows the reflected Bragg spectra from the optical fibers bonded to the main and aft spars. We used FBG interrogation monitors (I-MON 512 USB, Ibsen) to observe the reflected spectra and observed 30 FBGs in the wavelength domain. The Bragg wavelength intervals were set wider at shorter wavelengths. We aligned the FBGs with shorter Bragg wavelengths closer to the wing root as the wing root was expected to have greater strain variation amplitudes in general, and it was aimed at avoiding spectral overlap.

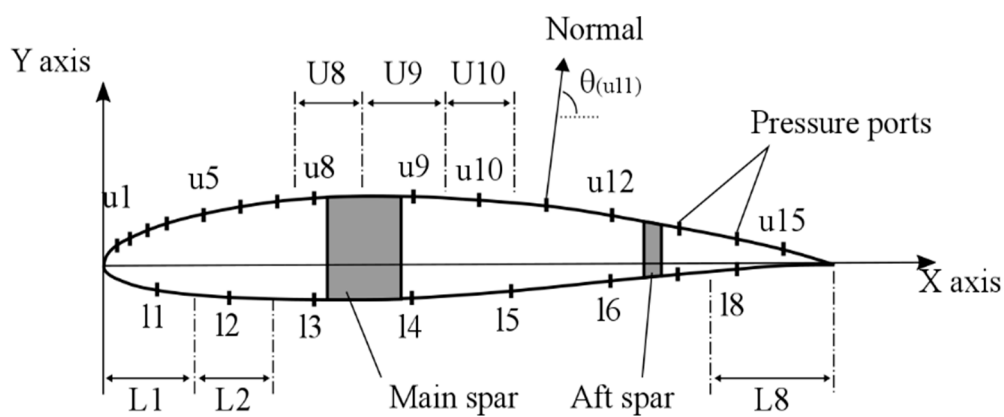
A wind shield was placed at the wing root. The lead wires of the servomotors, the pressure sensor tubes, and the optical fibers were routed to the basement of the wind tunnel and connected to the controller and the interrogators.



**Figure 1.** Wing model. **Left:** Photograph in wind tunnel taken from upstream and lower side of wing. **Right:** Schematic of flaps and sensors viewed from upper side of wing.

**Table 1.** Wing geometry.

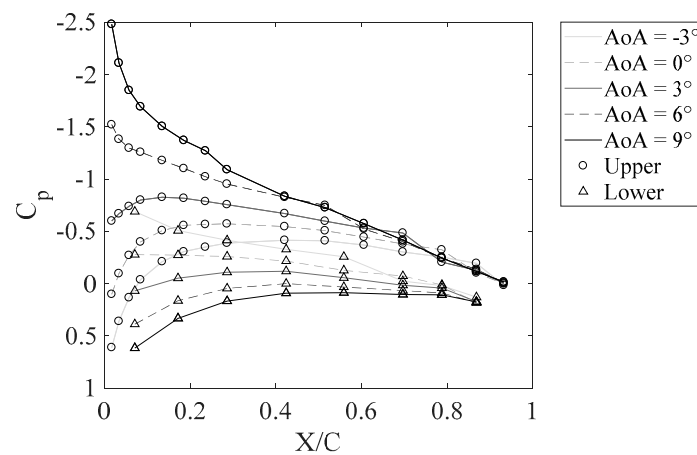
Segment No.	Position Z of Flap Center (m)	Span-Wise Flap Length (m)	Chord Length (mm)	Flap Width (mm)
1	0.277	0.472	297	54
2	0.749	0.472	283	51
3	1.221	0.472	271	48
4	1.686	0.458	258	45
5	2.144	0.458	243	43
6	2.602	0.458	226	40
7	3.025	0.388	208	39
8	3.413	0.388	186	37



**Figure 2.** Cross-section of wing model with locations of pressure ports and spars.

**Table 2.** Pressure port geometry. C represents chord length.

Port	Position X/C	Position Y/C	Normal Direction (deg)
(leading edge)	0	0	180
u1	0.02	0.024	125
u2	0.03	0.037	117
u3	0.06	0.047	110
u4	0.08	0.057	107
u5	0.13	0.067	102
u6	0.19	0.077	98
u7	0.24	0.084	96
u8	0.29	0.088	94
u9	0.42	0.088	90
u10	0.52	0.084	87
u11	0.61	0.077	84
u12	0.70	0.064	82
u13	0.79	0.047	80
u14	0.87	0.034	79
u15	0.93	0.020	77
b1	0.07	−0.030	260
b2	0.17	−0.040	267
b3	0.29	−0.044	270
b4	0.42	−0.040	273
b5	0.56	−0.034	275
b6	0.70	−0.020	276
b7	0.79	−0.013	276
b8	0.87	−0.0067	274
(trailing edge)	1	0	0
(main spar)	0.30–0.40	−0.043–0.091	-
(aft spar)	0.74–0.76	−0.017–0.057	-

**Figure 3.** Pressure coefficient distribution.

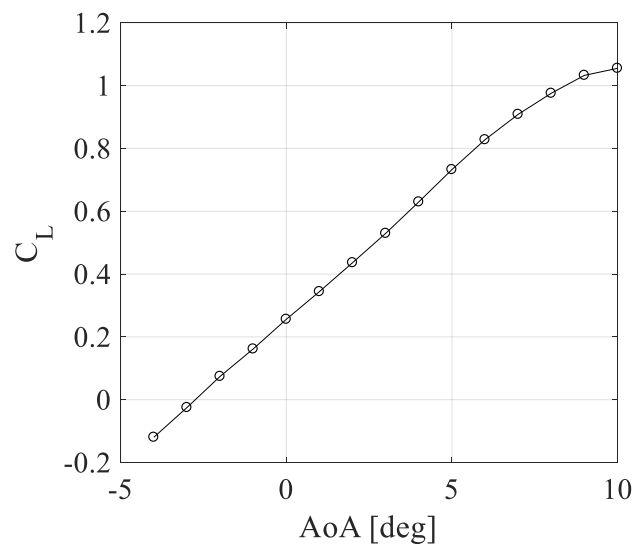


**Figure 4.** Lift coefficient versus AoA.

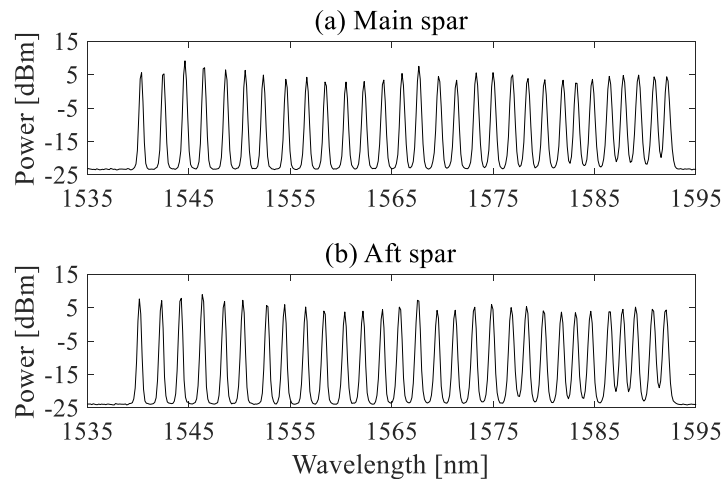


**Figure 5.** Reflected spectra from optical fiber sensors bonded along the main (a) and aft (b) spars.

## 2.2. Wind Tunnel Test

We applied aerodynamic loads to the wing model by wind tunnel tests. Figure 1 (left) is a photograph of the wing in the closed-circuit wind tunnel. The wind tunnel test section was 6.5 m high and 5.5 m wide. In this study, we defined the wind angle at the wing root as the AoA, and changed the AoA by rotating the turntable. A constant wind speed of 14 m/s and a dynamic pressure of 118.7 Pa were used in the following experiments. Reynolds number was  $2 \times 10^5$ .

A total of 586 test cases were conducted. The details of the test cases are presented in Table 3. Combinations of flap angles were used for each AoA case for the individual test types. The flap angles were maintained for approximately 10 s for each test case, and visual checks were conducted to ensure that there was no vibration on the wing model. In this manner, the measurements were performed without any dynamic effects. In the “aligned” test cases, all eight flap angles were set to  $0^\circ$ , and tests were conducted for 15 AoAs ranging from  $-4.0$ – $10.0^\circ$  with  $1^\circ$  intervals. In the “random” test cases, we aimed to apply 10 pseudo-random combinations of flap angles for 29 AoA cases ranging from  $-4.0$ – $10.0^\circ$  with  $0.5^\circ$  intervals. In order to avoid large changes in flap angles in a single test step that could result in large amplitudes of vibrations during testing, constant intervals of the flap angle variations between each test case were set, as presented in Table 4. We aimed to minimize the flap angle variation rate, specifically at the wing tip (i.e., Flap 8) where the greatest moments were caused.

Figure 6 shows examples of the Flaps 1, 4, and 7 angles for a number of the sequential “random” test cases. The flap angles “rebounded” within the range  $-15^{\circ}$ – $15^{\circ}$ . The bias remained in individual AoA cases (29 cases), although it was felt that the angle combinations were fully investigated across the 290 “random” case measurements. The primary aim of the “random” test cases was to obtain sufficient amounts of training data for the subsequent machine learning. In the “single” cases, a single flap was moved for eight AoAs ranging from  $-4.0$ – $10.0^{\circ}$  with  $2.0^{\circ}$  intervals. In the individual AoA cases, we moved a single flap through  $-15.0^{\circ}$ ,  $-5.0^{\circ}$ ,  $5.0^{\circ}$ , and  $15.0^{\circ}$  while the other flaps remained at  $0^{\circ}$  degrees. This sequence was repeated for all eight flaps. It was anticipated that the “single” test cases would highlight the effect of individual flaps on the aerodynamic load distributions. In “controlled” cases, a flap angle combination was applied as presented in Table 5. The flap angle combination was designed to reduce the moment while maintaining the lift force. The wing root tended to increase the lift force while the wing tip tended to decrease the moment. Measurements were conducted for 14 AoA cases ranging from  $-4.0$ – $10.0^{\circ}$  with  $1.0^{\circ}$  intervals. We did not conduct measurements at AoA =  $4.0^{\circ}$  as undamped wing vibration occurred. It was surmised that the vortex around the wing caused the resonance. The “controlled” cases were aimed at identifying the optimum load distribution control; therefore, it was regarded as the target data to be identified.

The efficiency of the acquisition of the training data is important from the practical point of view. The “aligned”, “random” and “single” test cases were designed to enable us to acquire data with simple maneuvers. It was only needed to pre-set the angle increments for single or all flaps between each test case, and the data was obtained automatically in individual test cases. There was no overlapping of the cases.

For each test case, the Bragg wavelengths, which correspond to the strains and pressures from which lift load distributions were calculated, were measured. We also recorded the AoA and eight flap angles.

Table 3. Test cases.

Type	AoA (deg)	Measurements at Each AoA (Total Measurements)
Aligned	$-4.0, -3.0, -2.0, -10.0$ (15 cases)	1 time (15 times)
Random	$-4.0, -3.5, -3.0, -10.0$ (29 cases)	10 times (290 times)
Single	$-4.0, -2.0, 0.0, -10.0$ (8 cases)	32 times (256 times)
Controlled	$-4.0, -3.0, -2.0, -10.0$ (14 cases *)	1 time (14 times)

\* We did not conduct measurements at AoA =  $4.0^{\circ}$ .

Table 4. Flap angle variation rate for “random” test cases.

Flap No.	Flap Angle Variation Rate (deg/test case)
1	9.8
2	7.2
3	5.7
4	4.8
5	3.6
6	2.6
7	1.9
8	1.2

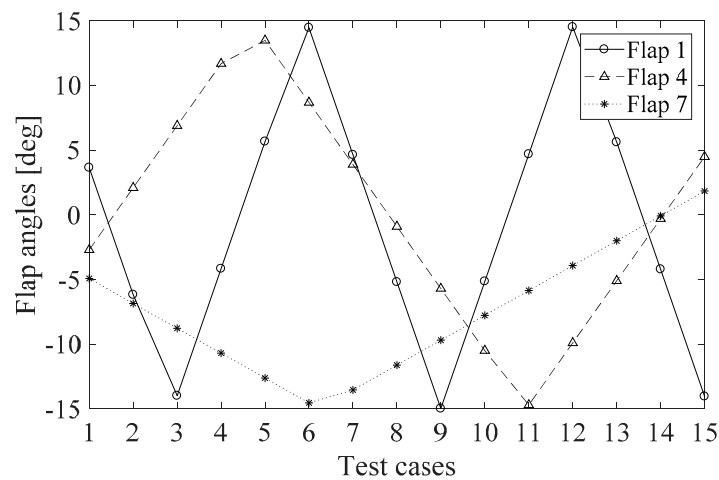


**Figure 6.** Examples of flap angles for “random” test cases.

**Table 5.** Flap angle combination for “controlled” test cases.

Flap No.	Flap Angle (deg)
1	15.0
2	15.0
3	13.0
4	0.8
5	−12.1
6	−15.0
7	−15.0
8	−15.0

### 2.3. Load Identification Method

For conceptual introduction, we first assume a simple linear elastic problem. Non-uniform distributed lift loads acting on the eight wing segments of the wing model, a load vector  $\mathbf{L}$ , induce strains at individual FBGs, strain vector  $\boldsymbol{\varepsilon}$ , which is expressed as

$$\boldsymbol{\varepsilon} = \mathbf{S}\mathbf{L}, \quad (1)$$

where  $\mathbf{S}$  is a transfer matrix. This is a direct problem where loads are input and strains are output. When applied loads are to be identified from measured strains, it is inversely solved as

$$\mathbf{L} = \mathbf{S}^+ \boldsymbol{\varepsilon}, \quad (2)$$

where  $\mathbf{S}^+$  is a generalized inverse matrix of  $\mathbf{S}$ . This solution tends to be unstable. In the neural network approach, a neural network is used to replace  $\mathbf{S}^+$  as

$$\mathbf{L} = \mathbf{NN}(\boldsymbol{\varepsilon}), \quad (3)$$

where  $\mathbf{NN}(x)$  expresses the output of a neural network when  $x$  was the input. In detail, an output of  $i$ th neuron in  $l$ th layer,  $a_i^{(l)}$ , is expressed by a weighted sum from the previous layer and a bias as

$$a_i^{(l)} = \sigma^{(l)} \left( \sum_j w_{ji}^{(l-1)} a_j^{(l-1)} + b_i^{(l)} \right), \quad (4)$$

where  $b_i^{(l)}$  is the bias of the  $i$ th neuron in the  $l$ th layer and  $w_{ji}^{(l-1)}$  is the weighted coefficient. The weight's subscript  $ji$  represents the link from the  $j$ th neuron in the  $(l-1)$ th layer to the  $i$ th neuron



in  $l$ th layer. The weighted sum with the bias is activated through the activation function  $\sigma$ . When a simple three-layer neural network is used, the  $i$ th element of  $\mathbf{L}$ ,  $L_i$ , is calculated from the strain input as

$$L_i = \left[ \sigma^{(3)} \left( \sum_j w_{ji}^{(2)} \left[ \sigma^{(2)} \left( \sum_k w_{kj}^{(1)} \varepsilon_k + b_j^{(2)} \right) \right] + b_i^{(3)} \right) \right]_i. \quad (5)$$

In this manner, the strain-to-load transfer can be represented by the neural network whose parameters are optimized through regression. This contributes to the stability of solutions [16]. In addition, the activation functions enable non-linear transformation, which enhances the applicability to a non-linear problem.

We created a neural network to calculate the lift load distribution. The architecture of the neural network, which was a feed-forward neural network with one hidden layer, is depicted in Figure 7. The input layer had 68 neurons, the hidden layer 12 neurons, and the output layer eight neurons, and they were fully-connected. The number of neurons and layers were determined experimentally. For the input layer, we used data from 60 FBGs bonded along the main and aft spars, as well as the data of the eight flap angles. It was evident that the strain had a mechanical cause-and-effect (or rather effect-and-cause) relationship and, therefore, the FBG signals should be used for load identification. Theoretically, the input of the strain information should be sufficient for the load identification as seen in Equations (3) and (5); however, it is anticipated that the strain variations would be less responsive with respect to local load variations specifically at the wing root due to the high stiffness. In order to enhance the responsiveness between the input and output of the neural network, the flap angle information was added as an input in this study. Therefore, the load identification process is redefined as

$$\mathbf{L} = NN_{load}(\varepsilon, \delta), \quad (6)$$

where  $\delta$  is the eight flap angles. The FBG signal, which is the Bragg wavelength shift from a reference condition, is typically converted to strain values by using a wavelength-strain coefficient; however, the physical unit was irrelevant in this instance of machine learning. Therefore, we used the raw Bragg wavelength shifts in wavelength units. The reference Bragg wavelengths were the resting state of the wing without wind. We used sigmoid transfer functions (hyperbolic tangent) in the hidden layer and a linear function in the output layer. The eight outputs corresponded to the lift load on the eight span-wise wing segments. The Levenberg–Marquardt backpropagation algorithm [25] was used as an optimizer, and the Nguyen–Widrow initialization method [26] was used to initialize weights and biases. The learning parameters used are identical to those used in a previous study [25].

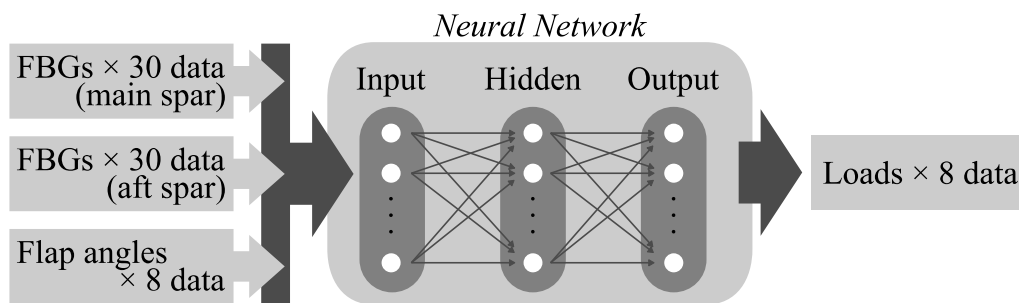


Figure 7. Architecture of neural network for load identification.

Test cases of “aligned”, “random”, and “single” were used as training data to train the neural network. The “controlled” cases were excluded so that they could be treated as new conditions for the neural network after training. For the training data, we used “aligned”, “single”, and 80% (232 cases) of the “random” test cases for optimization iterations. The balance of the “random” test cases was used for validation purposes in order to avoid overfitting. The loss of the validation data was monitored

during the optimization iterations. When the loss of the validation data increased across five sequential iterations, the optimization process was stopped and the weights and biases at the minimum loss were selected.

### 3. Results: Load Identification

Measurements were conducted for the planned test cases. As an example of the wing deformation, the measured strain distributions for  $\text{AoA} = -4^\circ$  and  $10^\circ$  in the “controlled” cases are shown in Figure 8. In order to better understand the mechanical implication of the data, we converted the measured Bragg wavelength shifts to strain values by using the Bragg wavelength-strain coefficient of  $827 \mu\epsilon/\text{nm}$ . The coefficient was experimentally calibrated in advance. In general, the amplitudes of strain variations were greater for the main spar than the aft spar due to the thickness difference under wing deflection. The strain amplitude was smaller at the wing tip, and this was in good agreement with typical strain distributions of a cantilever beam. However, the strain amplitude decreased at the wing root because of the greater cross-sectional area as well as the 400-mm stainless-steel shaft inserted at the wing root that increased the stiffness. The maximum strain amplitude was observed at approximately 400 mm. In the case of  $\text{AoA} = -4^\circ$ , it exhibited tensile strains, which indicated that the wing model deflected downward. In the case of  $\text{AoA} = 10^\circ$ , it exhibited compressive strains as the wing model deflected upward.

The neural network was trained using the measured data. Thereafter, we used the trained neural network to identify load distributions. Figure 9 shows examples of the load identification results for the test cases used to train the neural network. We plotted an “aligned” test case where  $\text{AoA} = 0^\circ$  and “single” test cases with  $\text{AoA} = -4^\circ$  and Flap 2 at  $15^\circ$ , and  $\text{AoA} = 4^\circ$  and Flap 7 at  $-15^\circ$ . In the “aligned” test case, the load distribution was relatively uniform, however, in the “single” test cases, load variations were observed at the repositioned flaps. The positive flap angle of Flap 2 at  $\text{AoA} = -4^\circ$  produced a lift increase, and the negative flap angle of Flap 7 at  $\text{AoA} = 4^\circ$  produced a decrease in lift. The lift variations were observed locally at the wing segments with the repositioned flaps. The three plots also indicated that greater  $\text{AoA}$  values produced greater lift loads. The solid lines represent the estimated loads and the dashed lines the applied loads that were calculated from the pressure values, and there is good agreement between them. This indicated that the neural network training was satisfactorily completed and the neural network could be applied to the load identification problem. In order to examine the neural network performance for new conditions, we input the FBG and flap angle data of the “controlled” test cases, which were not used for the training. Figure 10 shows the load identification results for  $\text{AoA} = -4^\circ$  and  $10^\circ$ . It could be seen that for the “controlled” flap angles, the wing root was subjected to greater lift loads and the wing tip to smaller or negative lift loads. The total lift loads increased with increasing  $\text{AoA}$ . The solid lines represent the estimated loads and the dashed lines the applied loads. The results were in good agreement, which indicated that the neural network successfully learned to generalize unexperienced conditions. The errors appeared greater for the data not used for training, and thus for a quantitative comparison, we plotted the estimated loads with regard to the applied loads in Figure 11. The load values correspond to the lift loads on the individual wing segments. The black circles represent the results for the training data that includes the “aligned,” “random,” and “single” test cases. The red squares represent the results for other data, the “controlled” test cases. The error ranges were from  $-0.89$ – $0.84$  N and from  $-1.5$ – $1.4$  N for the training and other data, respectively. The standard deviations of the errors were  $0.14$  N and  $0.57$  N for the training and other data, respectively. The slight difference of the accuracy between the training and other data reflected that the neural network output better results for the data used for training. This also indicated that the load identification performance would be improved by adding load cases of interest to training data set.

In the experiment, the out-of-plane forces of the wing model were identified as the lift loads. On the other hand, the in-plane forces were applied to the wing model, which were out of focus in this study. The applied in-plane forces were unavailable because the in-plane force consisted of the in-plane

component (X-component in Figure 2) of the pressure values and the friction drag, which were difficult to directly and accurately measure simply by the equipped pressure ports. If the applied in-plane forces were measured and the training data were prepared, the in-plane forces would potentially be identified through the same identification process. By identifying both the out-of-plane and in-plane forces of the wing, the lift and drag forces for aircraft would be estimated.

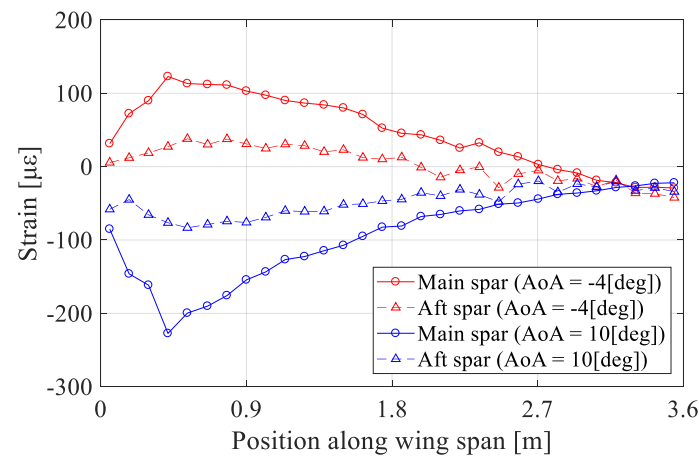


**Figure 8.** Measured strain distributions at  $\text{AoA} = -4^\circ$  and  $10^\circ$  in “controlled” test cases.

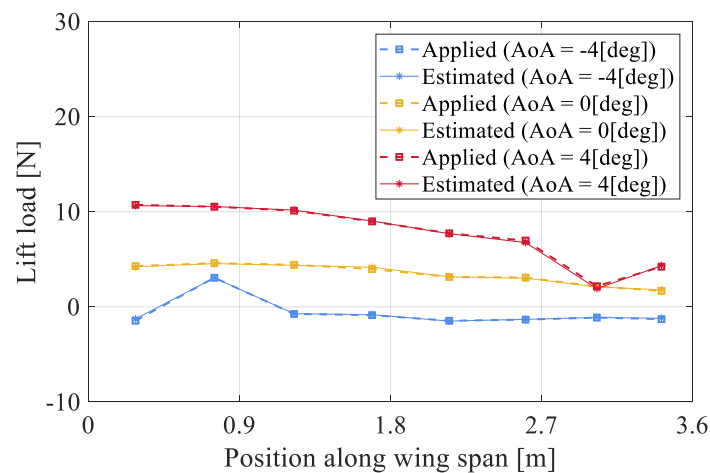


**Figure 9.** Load identification results in “aligned” test case ( $\text{AoA} = 0^\circ$ ) and “single” test case ( $\text{AoA} = -4^\circ$  and  $4^\circ$ ). Flap 2 angle  $15^\circ$  when  $\text{AoA} = -4^\circ$ , and Flap 7 angle  $-15^\circ$  when  $\text{AoA} = 4^\circ$ .

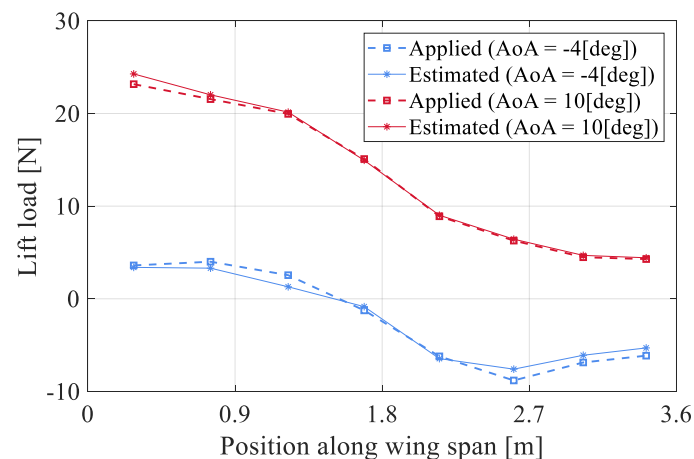


**Figure 10.** Load identification results in “controlled” test cases with  $\text{AoA} = -4^\circ$  and  $10^\circ$ .

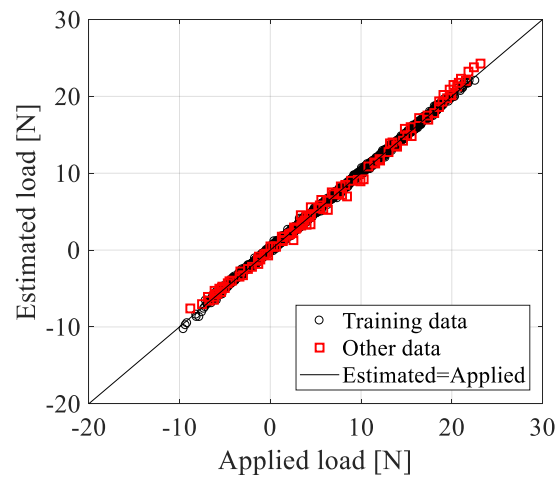


Figure 11. Comparison between applied and estimated loads.

#### 4. Discussion: AoA Identification

Loads were identified by solving the mechanical problems as in Equations (1)–(6). At the same time, the lift load distribution,  $L$ , is in an aerodynamic problem as

$$L = qC_L(\delta, \alpha)A, \quad (7)$$

where  $q$  is the dynamic pressure,  $\alpha$  is the AoA,  $C_L$  is the lift coefficients, and  $A$  is the areas of the wing segments. In the experiment, we could assume that the dynamic pressure  $q$  and the wing areas  $A$  were constant, and the  $C_L$  was a function of the flap angles  $\delta$  and the AoA  $\alpha$ . The variables in the aerodynamic problem were the lift loads  $L$ , the flap angles  $\delta$ , and the AoA  $\alpha$ . Considering that the flap angles are observable and the lift loads are now identified, it was anticipated that the AoA could be theoretically and practically solved by setting  $L$  and  $\delta$  as inputs as

$$\alpha = NN(L, \delta). \quad (8)$$

In this case again, the regression nature of the neural network approach would enhance the stability of solutions. Furthermore, the non-linear transformation is beneficial specifically because the aerodynamic problems show non-linearity.

We designed a neural-network-based identification process for the AoA as shown in Figure 12. In this design, we identify load distributions by using the 60 FBGs (strain) and flap angle data through the neural network for the load identification as discussed above, and thereafter we identify the AoA by using the identified load distribution and the flap angles through another neural network for the AoA identification. This process requires only the FBG and flap angle data to be observed, which is a feasible assumption.

The neural network for the AoA identification had one hidden layer with 10 neurons, which was determined experimentally. We set other properties and training parameters in the same way as the load identification. In order to train the neural network for the AoA identification, we prepared a dataset of flap angles and estimated loads, which were the output from the neural network for the load identification for the training test cases (“aligned,” “random,” and “single”). The other cases (“controlled”) were used to check the performance from the new conditions.

Figure 13 shows the results of the neural network AoA predictions. The good agreement between the applied and estimated AoAs indicated the theoretical validation of the AoA identification approach. The error ranges were from  $-0.78$ – $0.46^\circ$  and from  $-1.03$ – $0.16^\circ$  for the training and other data, respectively. The standard deviations of the errors were  $0.15^\circ$  and  $0.38^\circ$  for the training and other data, respectively.

Because of limitations of the experimental setup, we defined and observed the AoA as the turntable angle. If we could measure the profile of the AoA along the wing span, the neural network approach might be capable of identifying local AoAs, which would contribute to the development of effective wing twist techniques.

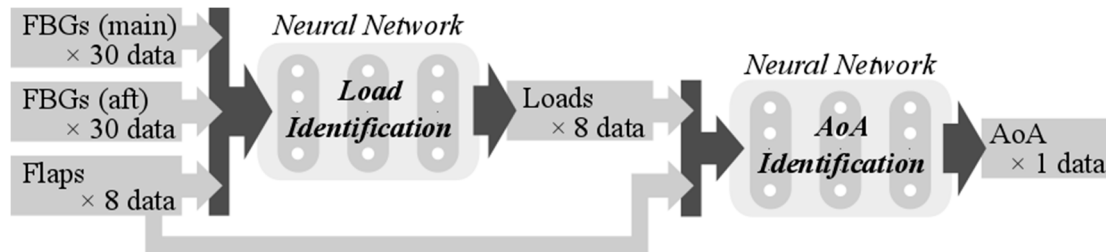


Figure 12. Design of NN-based identification process for load and AoA.

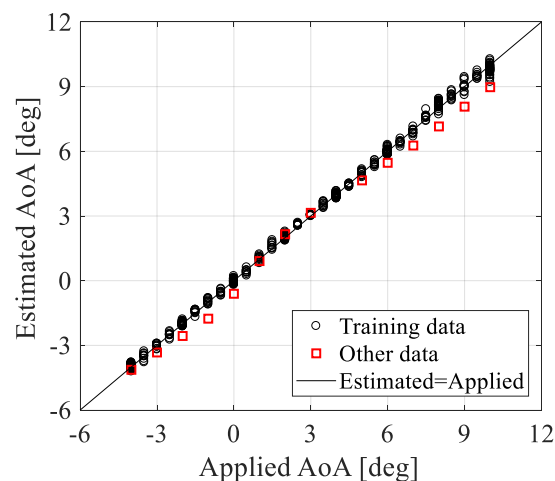


Figure 13. Comparison between applied and estimated AoA.

## 5. Conclusions

We integrated the optical fiber sensing technique and the neural network approaches, and investigated the applicability for loads and AoAs identification of wing structures.

We developed a 3.6-m semi-spanned wing model with eight trailing edge flaps. Two optical fibers with 30 FBGs were bonded on the upper side of the wing model along the main and aft spars. Aerodynamic loads were applied to the wing model by wind tunnel tests, and load identification was performed by using the neural network approach. The FBG data and eight flap angles were input to the neural network, and the estimated load distributions on the eight wing segments were output. The load distributions were successfully identified, even for data that were not used for training of the neural network. The error range was from  $-1.5$ – $1.4$  N with a standard deviation of 0.57 N.

We solved the mechanical inverse problem by using the neural network. We also investigated the application of the neural network to solve the aerodynamic problem to identify the AoA. In this process, load distributions were first identified, and thereafter the AoA was determined by using the load distributions and the flap angles through another neural network. This process required only the FBG and flap angle data to be observed. The neural network successfully identified the AoA with error ranges from  $-1.03$ – $0.46^\circ$  with a standard deviation of  $0.38^\circ$ .

**Author Contributions:** D.W. proposed the idea, and conducted the simulation and analysis. The experiment was conducted by D.W. and M.T. The article was written and completed by D.W., and checked by M.T.

**Funding:** This research was funded by JSPS KAKENHI, grant number JP17K14878.

**Conflicts of Interest:** The authors declare no conflict of interest.

## References

1. Nguyen, N.; Ting, E.; Chaparro, D.; Drew, M.; Swei, S. Multi-objective flight control for drag minimization and load alleviation of high-aspect ratio flexible wing aircraft. In Proceedings of the 58th AIAA/ASCE/AHS/ASC Structures, Structural Dynamics, and Materials Conference, Grapevine, TX, USA, 9–13 January 2017. [\[CrossRef\]](#)
2. Tang, D.; Dowell, E.H. Experimental and theoretical study on aeroelastic response of high-aspect-ratio wings. *AIAA J.* **2001**, *39*, 1430–1441. [\[CrossRef\]](#)
3. Tang, D.; Dowell, E.H. Experimental and theoretical study of gust response for high-aspect-ratio wing. *AIAA J.* **2002**, *40*, 419–429. [\[CrossRef\]](#)
4. Tang, D.; Grasch, A.; Dowell, E.H. Gust response for flexibly suspended high-aspect ratio wings. *AIAA J.* **2010**, *48*, 2430–2444. [\[CrossRef\]](#)
5. Mohamed, A.; Massey, K.; Watkins, S.; Clothier, R. The attitude control of fixed-wing MAVs in turbulent environments. *Prog. Aerosp. Sci.* **2014**, *66*, 37–48. [\[CrossRef\]](#)
6. Mohamed, A.; Clothier, R.; Watkins, S.; Sabatini, R.; Abdulrahim, M. Fixed-wing MAV attitude stability in atmospheric turbulence, part 1: Suitability of conventional sensors. *Prog. Aerosp. Sci.* **2014**, *70*, 69–82. [\[CrossRef\]](#)
7. Mohamed, A.; Watkins, S.; Clothier, R.; Abdulrahim, M.; Massey, K.; Sabatini, R. Fixed-wing MAV attitude stability in atmospheric turbulence, part 2: Investigating biologically-inspired sensors. *Prog. Aerosp. Sci.* **2014**, *71*, 1–13. [\[CrossRef\]](#)
8. Tarantola, A. *Inverse Problem Theory and Methods for Model Parameter Estimation*; SIAM: Philadelphia, PA, USA, 2005; ISBN 978-0898715729.
9. Hansen, P.C. *Discrete Inverse Problems: Insight and Algorithms*; SIAM: Philadelphia, PA, USA, 2010; ISBN 978-0898716962.
10. Aster, R.C.; Borchers, B.; Thurber, C.H. *Parameter Estimation and Inverse Problems*, 2nd ed.; Academic Press: Cambridge, MA, USA, 2012; ISBN 978-0123850485.
11. Shkarayev, S.; Krashantisa, R.; Tessler, A. An inverse interpolation method utilizing in-flight strain measurements for determining loads and structural response of aerospace vehicles. In Proceedings of the 3rd International Workshop on Structural Health Monitoring, Stanford, CA, USA, 12–14 September 2001.
12. Coates, C.W.; Thamburaj, P. Inverse method using finite strain measurement to determine flight load distribution functions. *J. Aircr.* **2008**, *45*, 366–370. [\[CrossRef\]](#)
13. Nakamura, T.; Igawa, H.; Kanda, A. Inverse identification of continuously distributed loads using strain data. *Aerosp. Sci. Technol.* **2012**, *23*, 75–84. [\[CrossRef\]](#)
14. Cao, X.; Sugiyama, Y.; Mitsui, Y. Application of artificial neural networks to load identification. *Comput. Struct.* **1998**, *69*, 63–78. [\[CrossRef\]](#)
15. Trivailo, P.M.; Carn, C.L. The inverse determination of aerodynamic loading from structural response data using neural networks. *Inverse Prob. Sci. Eng.* **2006**, *14*, 379–395. [\[CrossRef\]](#)
16. Wada, D.; Sugimoto, Y.; Murayama, H.; Igawa, H.; Nakamura, T. Investigation of inverse analysis approach and neural network approach for distributed load identification using distributed strains. *Trans. Jpn. Soc. Aeronaut. Space Soc.* **2019**, *62*.
17. Carpenter, T.J.; Albertani, R. Aerodynamic load estimation from virtual strain sensors for a pliant membrane wing. *AIAA J.* **2015**, *53*, 2069–2079. [\[CrossRef\]](#)
18. Wada, D.; Igawa, H.; Kasai, T. Vibration monitoring of a helicopter blade model using the optical fiber distributed strain sensing technique. *Appl. Opt.* **2016**, *55*, 6953–6959. [\[CrossRef\]](#) [\[PubMed\]](#)
19. Wada, D.; Igawa, H.; Tamayama, M.; Kasai, T.; Arizono, H.; Murayama, H. Flight demonstration of aircraft wing monitoring using optical fiber distributed sensing system. *Smart Mater. Struct.* **2019**, *28*, 055007. [\[CrossRef\]](#)
20. Pak, C. Wing shape sensing from measured strain. *AIAA J.* **2016**, *54*, 1064–1073. [\[CrossRef\]](#)
21. Kim, J.; Park, Y.; Kum, Y.; Shrestha, P.; Kim, C. Aircraft health and usage monitoring system for in-flight strain measurement of a wing structure. *Smart Mater. Struct.* **2015**, *24*, 105003. [\[CrossRef\]](#)

22. Kressel, I.; Balter, J.; Mashiach, N.; Sovran, I.; Shapira, O.; Shemesh, N.Y.; Glamm, B.; Dvorjetski, A.; Yehoshua, T.; Tur, M. High speed, in-flight structural health monitoring system for medium altitude long endurance unmanned air vehicle. In Proceedings of the 7th European Workshop on Structural Health Monitoring, Nantes, France, 8–11 July 2014.
23. Lance, R.; Allen, R.P., Jr.; Anthony, P.; Patrick, C.; Harmory, P.; Pena, F. *NASA Armstrong Flight Research Center (AFRC). Fiber Optic Sensing System (FOSS) Technology*; NASA Technical Reports Server: Edwards, CA, USA, 2014.
24. Kersey, A.D.; Davis, M.A.; Patrick, H.J.; LeBlanc, M.; Koo, K.P.; Askins, C.G.; Putnam, M.A.; Friebele, E.J. Fiber grating sensors. *J. Lightwave Technol.* **1997**, *15*, 1442–1463. [[CrossRef](#)]
25. Hagan, M.T.; Menhaj, M.B. Training feedforward networks with the Marquardt algorithm. *IEEE Trans. Neural Netw.* **1994**, *5*, 989–993. [[CrossRef](#)] [[PubMed](#)]
26. Nguyen, D.; Widrow, B. Improving the learning speed of 2-layer neural networks by choosing initial values of the adaptive weights. In Proceedings of the 1990 IJCNN International Joint Conference on Neural Networks, San Diego, CA, USA, 17–21 June 1990.



© 2019 by the authors. Licensee MDPI, Basel, Switzerland. This article is an open access article distributed under the terms and conditions of the Creative Commons Attribution (CC BY) license (<http://creativecommons.org/licenses/by/4.0/>).